Growth, SHG, Z-scan, optical limiting and quantum chemical investigation of hexamethylenetetraminium hydrogen DL-malate – An organic crystal for optoelectronic applications

M. Saravanakumar [a], J. Chandrasekaran [a,*], M. Krishnakumar [b], Merin George [c], G. Vinitha [d], Mohd Anis [e]

[a] Crystal Research Laboratory, Department of Physics, Sri Ramakrishna Mission Vidyalaya College of Arts and Science, Coimbatore, 641 020, Tamil Nadu, India
[b] Department of Physics, University College of Engineering, Dindigul, 624 622, India
[c] Post Graduate & Research Department of Physics, Bishop Moore College, Mavelikara, Kerala, 690 110, India
[d] Division of Physics, School of Advanced Sciences, VIT Chennai, Chennai, 600 127, Tamil Nadu, India
[e] Department of Physics and Electronics, Maulana Azad College of Arts, Science and Commerce, Aurangabad, 431001, Maharashtra, India

HIGHLIGHTS

- Hexamethylenetetraminium hydrogen DL-malate (HMTM) as an efficient material for NLO applications.
- The HMTM exhibits low dielectric constant, dielectric loss and positive photoconductivity.
- The relative powder SHG efficiency of HMTM has 1.25 times greater than that of KDP.
- The HMTM possess self-defocusing nature and the optical limiting response.

ARTICLE INFO

ABSTRACT

Single crystals of hexamethylenetetraminium hydrogen DL-malate (HMTM) have been successfully synthesized by slow evaporation method and structurally analyzed by single crystal X-ray diffraction, powder X-ray diffraction, FTIR, FT-Raman, ^{1}H and ^{13}C NMR spectroscopic techniques. These investigations confirm the formation of HMTM crystal which crystallize in the non-centrosymmetric space group Cc with monoclinic crystal system. The N–H···O and O–H···O intermolecular hydrogen bonding interactions have been investigated by Hirshfeld surface analysis. The optical absorption cut-off wavelength of the grown crystal is observed at 353 nm in the UV–visible spectrum. From the photoluminescence spectrum, two intense emission peaks are identified at 312 nm and 415 nm. Dielectric study reveals low values of dielectric constant and dielectric loss. The positive photoconducting nature of HMTM is identified from the photoconductivity analysis. Second harmonic generation efficiency of the powdered HMTM is found to be 1.25 times greater than that of powdered KDP. The Z-scan and optical limiting results indicate that HMTM exhibits self-defocusing nature and optical limiting response, respectively. In addition, charge transfer interactions, first- and second-order hyperpolarizability values are computed by density functional theory calculations and are discussed in detail.

1. Introduction

Recently, researchers pay profound attention in the design, growth and development of single crystalline materials from organic complexes which exhibit superior nonlinear optical (NLO) efficiencies than their inorganic counterparts [1–4]. Organic NLO complexes possess significant properties thereby routing them in to vital applications in the fields of optical storage, frequency mixing, signal processing, Terahertz frequency generation etc. Mostly, complexes formed from the association of dicarboxylic acids with other organic molecules result in residues containing notable existence of higher order nonlinearities [5]. The underlying effects of molecular arrangements in organic complexes

result in hydrogen bonding mechanism ranging from strong to very strong levels, which firmly enhance their nonlinear optical behavior [5]. In general organic complexes designed from di-carboxylic acids blended with other organic molecules exhibit extreme structural flexibility pertaining to the ability in optimization of higher order NLO properties. Also, the formation of organic charge transfer complexes have been meticulously studied owing to the special kind of interaction among donors and acceptors. Additionally, the process of protonation of donor molecules from acceptors in organic NLO complexes is the basis for hydrogen bonding formation [6–10].

In the recent past, the intramolecular charge transfer interaction and second harmonic generation efficiency of some hexamethylenetetramine phenol derivatives [11] have been already reported. The crystal structure, thermal, Hirshfeld surface analysis and quantum chemical calculations of the aniline and hexamethylenetetramine dicarboxylic acid complexes [12] have been studied. The vibrational assignments of hexamethylenetetramine [13] and its halogen adducts [14] have been investigated. Earlier, the crystal structure and its enhanced anomeric interactions of the hexamethylenetetramine hydrogen DL-malate and some acid derivatives were reported by Sosale Chandrasekhar and co-workers [15]. From a concise literature survey, we have observed that no significant analyses were reported for hexamethylenetetraminium hydrogen DL-malate (HMTM).

In the present study, an organic–organic charge transfer complex hexamethylenetetraminium DL-malate (HMTM) has been synthesized and single crystals of the complex have been grown by solution growth technique. The prime aim of the present investigation is to examine the reaction mechanism resulting from hydrogen bond formation between starting materials and the possibilities of growing the resultant complex as a single crystalline material for NLO applications. Furthermore, the physical properties of the HMTM employing techniques like powder X-ray diffraction, ^{1}H, ^{13}C NMR, FTIR, FT-Raman, optical absorption, photoluminescence, dielectric study, photoconductivity, second harmonic generation (SHG), Z-scan, optical limiting, as well as quantum chemical density functional theory (DFT) calculations, natural bonding orbital, frontier molecular orbital, natural population charge, electrostatic potential map, first- and second-order hyperpolarizabilities and Hirshfeld surface analysis are investigated and these characterizations have been reported for the first time in this work.

2. Crystal synthesis and growth

The HMTM crystal was prepared by adding the hexamethylenetetramine and DL-malic acid in the equimolar ratio (1:1) in methanol solution. The solution was filtered and kept to dry at room temperature. The synthesized crystals were further purified by repeated recrystallization in methanol solvent. In this process, optically transparent HMTM single crystal ($C_6H_{13}N_4^+.C_4H_5O_5^-$) of size 8 x 4 x 2 mm^3 was formed after a period of 3 weeks (Fig. 1a). The reaction mechanism of HMTM is shown in Scheme 1.

2.1. Experimental techniques

The single crystal X-ray diffraction analysis of the HMTM crystal was carried out using graphite-monochromated MoKα radiation (λ = 0.71073 Å) in the scanning range of 10–80° at 293 K by means of an Enraf-Nonius CAD-4 diffractometer and powder X-ray diffraction study was performed by CuKα radiation (λ = 1.5405 Å) using RICH SIEFERT X-ray powder diffractometer. The ^{1}H and ^{13}C NMR spectra of the HMTM were carried out by Bruker 400 MHz Spectrometer using deuterated dimethyl sulfoxide solvent (DMSO). The Fourier transform infrared (FTIR) and Fourier transform Raman (FT-Raman) spectra of HMTM in methanol solvent were recorded using a JASCO (FT/IR-4600typeA) spectrometer and a BRUKER RFS 27 spectrometer, respectively. UV–visible spectrum was recorded by JASCO V-770 instrument in the range of 200–900 nm using methanol as solvent. The
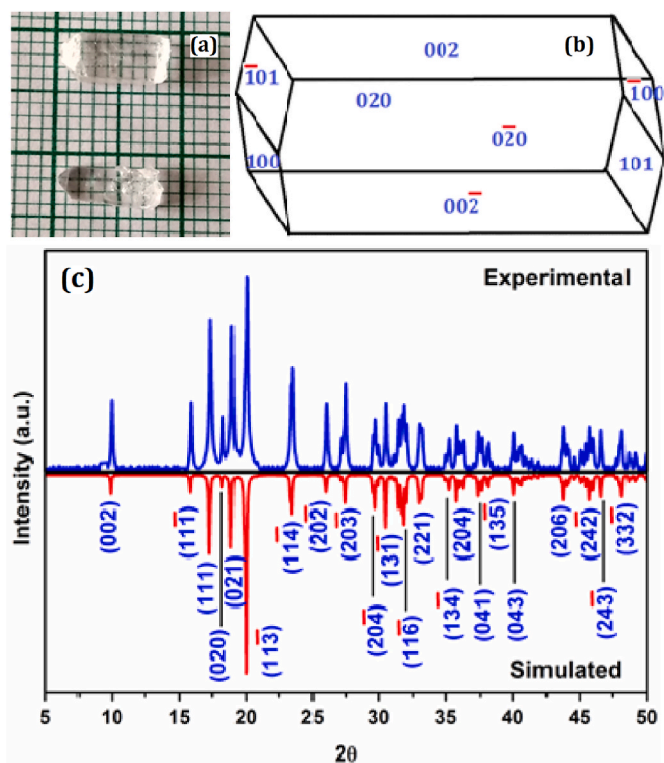
Fig. 1. (a) Crystal image of HMTM. **(b)** BFDH figure of HMTM. **(c)** Simulated and experimental powder XRD pattern of HMTM.

photoluminescence spectrum of HMTM was recorded by a JASCO FP-8300 spectrometer using methanol solvent. Dielectric analysis was carried out in the frequency range of 50 Hz-5MHz at 303–383 K temperatures using Hioki 3532-50 LCR meter. Photoconductivity measurement of HMTM crystal was carried out by Keithley-6517B electrometer. A Q-switched Nd:YAG laser with wavelength of 1064 nm was used to measure the second harmonic generation (SHG) efficiency of powdered HMTM crystal. Z-scan and optical limiting analyses were performed with the support of continuous wave Nd:YAG laser of 532 nm wavelength.

2.2. Computational techniques

The quantum chemical calculations of HMTM have been carried out using DFT/Becke-3-Lee-Yang-Parr (B3LYP)/6-311++G(d,p) level of theory in Gaussian 09 W program package [16–18]. The isolated HMTM molecule is optimized in methanol solvent phase and its optimized molecular structure is used for other DFT calculations. The natural bonding orbital (NBO), intramolecular charge transfer interactions have been computed by NBO 3.1 program [19–21]. The frontier molecular orbitals and molecular electrostatic potential (MEP) surfaces are plotted using GaussView 5.0 visualization software [22]. The Crystal Explorer 3.1 [23] software package was used to plot three-dimensional Hirshfeld surface of the HMTM molecule.

3. Results and discussion

3.1. X-ray diffraction studies

The HMTM crystal is found to crystallize in the monoclinic crystal system with non-centrosymmetric space group Cc. The cell dimensions are evaluated as a = 6.983(3) Å, b = 9.721(3) Å and c = 18.214(8) Å. This is in good agreement with the reported value [15], are compared in Table 1. The number of HMTM molecules present per unit cell (Z) is 4, it
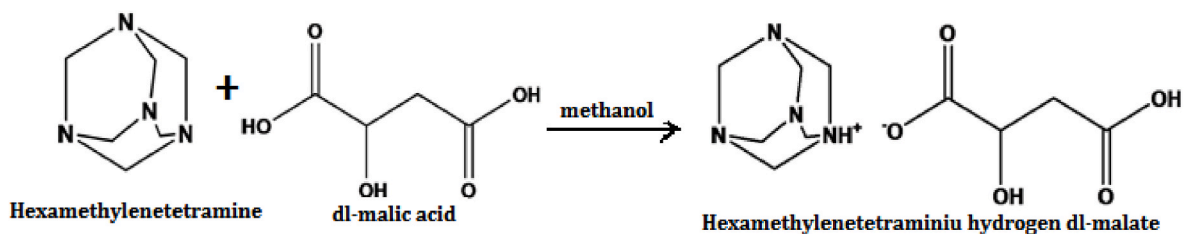
Scheme 1. Schematic diagram of HMTM synthesis.

Table 1
Comparative analysis of lattice parameters of HMTM.

Cell Lengths	Present Study	Reference [15]
A	6.983	6.983
B	9.721	9.716
C	18.214	18.209

contains an equal number of hexamethylenetetramine cations and DL-malate anions and the unit cell volume (V) is 1208.32 Å^3. The BFDH morphology of the HMTM is shown in Fig. 1b. The powder X-ray diffraction (PXRD) pattern of the HMTM agrees well with the simulated PXRD pattern from corresponding single crystal X-ray diffraction data [15], representing the successful growth of the HMTM crystal. The recorded and simulated PXRD patterns are compared and illustrated in Fig. 1c. The crystalline nature of the HMTM has been identified from sharp diffraction peaks.

3.2. NMR spectral analysis

The proton and carbon signals in the NMR spectra confirm the crystal structure of HMTM. The recorded ^{1}H and ^{13}C NMR spectra are illustrated in Fig. 2a and b. The singlet proton signal at $\delta = 4.993$ ppm is due to the H$_a$ atom of the carboxylic acid in the DL-malate moiety. The intense singlet proton signal at $\delta = 3.929$–3.958 ppm has been assigned to H$_c$ atoms of the NH$^+$ group adjacent to the methylene group and methine group. The broad hump proton signal that occur in the upfield region at $\delta = 4.420$ ppm is associated with the overlapped OH and NH$^+$ groups. The singlet proton signal at $\delta = 2.931$ ppm is attributed to methylene group H$_d$ atoms of the hexamethylenetetraminium moiety. The doublet proton signal at $\delta = 2.246$–2.289 ppm is assigned to the methylene group H$_b$ atom of the DL-malate moiety. The distinct carbon signals at $\delta = 80.53$ ppm, attributed to C2 carbon atoms, is down shifted due to the attached NH$^+$ group and $\delta = 70.75$ ppm is due to C1 carbon atoms of the hexamethylenetetraminium moiety. The downfield carbon signals at $\delta = 177.93$ ppm and $\delta = 174.90$ ppm are attributed to the highly unshielded C3 carbon atom of carboxylate group and C6 carbon atom of the carboxylic acid in DL-malate moiety. The NMR shift at $\delta = 68.20$ ppm confirms the presence of hydroxyl group attached to the C4
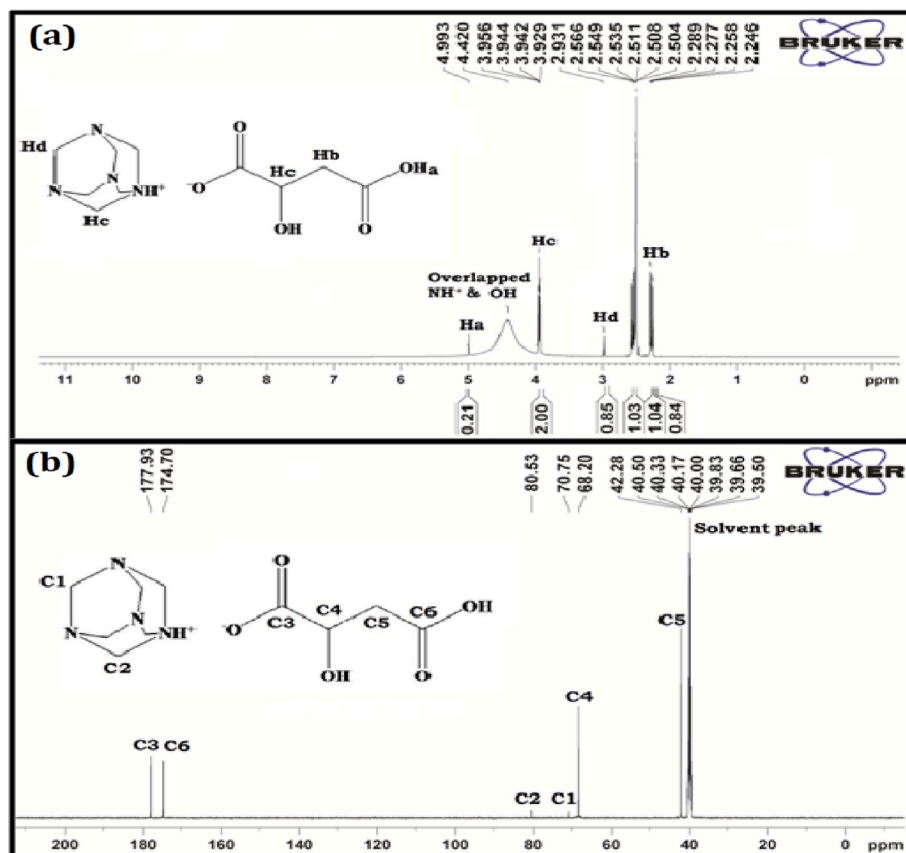
Fig. 2. (a–b). Experimental ^{1}H and ^{13}C NMR spectra of HMTM.

carbon atom and $\delta = 42.28$ ppm is attributed to the C5 carbon atom of the DL-malate moiety.

3.3. Structural geometry study

The optimized molecular structure with atomic numbering of an isolated HMTM molecule is illustrated in Fig. 3. The bond lengths of O4···H15 and O5···H1 are found to be 1.572 Å and 1.454 Å, respectively, which are considerably lesser than that of its van der Waal's radii (2.72 Å). This confirms the existence of N16–H15···O4 and O7–H1···O5 hydrogen bonding within the HMTM molecule. Due to hydrogen bonding, the bond distance of protonated N16–H15 is found to be 1.074 Å and that of O7–H1 is found to be 1.054 Å, which are slightly increased due to electron delocalization. The bond angles of C12–O4–H15 (129.22°), C8–C9–C13 (116.45°) and H1–O7–C8 (112.46°) are decreased compared to the experimental values of 123.38°, 117.95° and 108.35°, respectively. The computed bond angle of O4–H15–N16 (167.88°) is larger than that of the XRD value (149.26°). The bond distance of N16–C17, N16–C20 and N16–C35 are calculated to be 1.542 Å, 1.545 Å and 1.543 Å, respectively. These bond distances are slightly larger than that of other N–C bond distances (~1.46–1.49 Å) in the HMTM molecule and the bond angles of C17–N16–C20, C17–N16–C35 and C20–N16–C35 are observed to be 108.52°, 108.52° and 108.46°, respectively. This is slightly lesser than that of other C–N–C bond angles (~109°) due to the N16–H15···O4 hydrogen bonding interaction. The dihedral angle of C12–O4–H15–N16 is found to be −163.61°, which is slightly compressed due to hydrogen bonding interaction and high charge delocalization in the σ*(N16–H15) anti-bonding orbital (0.112e). In the hexamethylenetetraminium moiety, the dihedral angles for O4–H15–N16–C17 (−11.21°), O4–H15–N16–C20 (108.64°) and O4–H15–N16–C35 (−131.56°) are increased compared to the experimental values due to N16–H15···O4 hydrogen bonding interaction and hyperconjucative interaction between lone pair nO4 orbital and σ* (N16–H15) anti-bonding orbital. The optimized geometric parameters of bond length and angles are listed in Table 2. The calculated structural parameters are in good agreement with the XRD value.

3.4. Hirshfeld surface analysis

Hirshfeld surface of HMTM provides the graphical visualization figure for understanding the intermolecular interactions. The intermolecular contacts of the molecule are related to van der Waal's (vdw) radii using red-white-blue colour format. The three-dimensional d_{norm} Hirshfeld surface of intermolecular interactions are mapped in the range from $d_e = -0.585$ to $d_i = 1.318$ Å as shown in Fig. 4a. In the d_{norm} Hirshfeld surface, the red spot over the surface indicates N–H···O and O–H···O hydrogen bond, white spot indicates close intercontacts near the vdw radii and longer intercontacts with vdw radii is indicated by blue colour. The O···H bond distance of N–H···O (1.183–2.141 Å) and O–H···O (1.525–1.851 Å), which are lesser than the O···H vdw radii confirm the presence of N–H···O and O–H···O hydrogen bonding
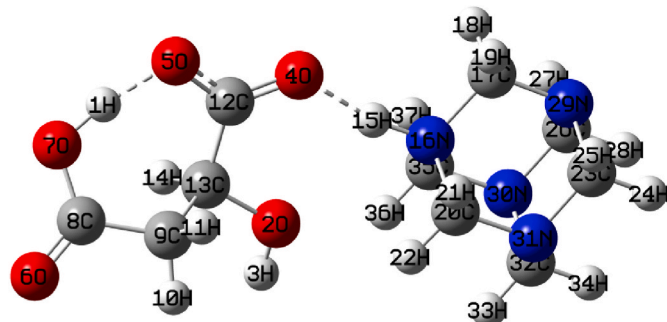
Fig. 3. Optimized structure of HMTM.

contacts in the title molecule. From Fig. 4b, the combination of d_e and d_i in the mapping of the two-dimensional fingerprint plot of the HMTM molecule indicates the contribution of inside and outside elements and its reciprocal intercontacts, H···H/H···H (45.7%), O···H/H···O (40.9%), N···H/H···N (9.4%), C···H/H···C (1.4%), C···O/O···C (0.8%), N···C/C···N (0.8%) and O···O/O···O (0.7%) of the total Hirshfeld surface area.

3.5. Vibrational spectral analyses

The FTIR and FT-Raman vibrational spectrum of the HMTM is illustrated in Fig. 5a and b, and their distinctive vibrational assignments are listed in Table 3.

3.5.1. Hexamethylenetetraminium vibration

The NH+ stretching vibrations occurs at weak band at 3350-3100 cm^{-1} [24]. The NH+ stretching of HMTM is red shifted and it is observed as a weak band at 3108 cm^{-1} in FT-Raman spectrum. This NH+ stretching wavenumber shift indicates the presence of N–H+ ... O− intermolecular hydrogen bonding within HMTM. The NH+ scissoring in-plane deformation vibration is found at 1513 cm^{-1} and 1588 cm^{-1} in the FTIR spectrum. The NH + rocking and wagging out of plane deformation vibrations are observed at 1006 cm^{-1} and 729 cm^{-1} in FTIR and FT-Raman spectrum, respectively. The CH$_2$ asymmetric and symmetric stretching vibrational modes generally occur in the range 2940–2915 cm^{-1} and 2870-2840 cm^{-1}, respectively. In tertiary amines, CH$_2$ stretching is shifted to about 2800 cm^{-1} when a nitrogen atom is present next to CH$_2$ group [25,26]. The CH$_2$ asymmetric and symmetric stretching bands are observed at 2954 cm^{-1} and 2803 cm^{-1} respectively, in the FTIR spectrum. The CH$_2$ scissoring deformation vibrational band is observed at 1445 cm^{-1} in the FTIR spectrum. The CH$_2$ rocking in-plane deformation vibration is found at 783 cm^{-1} in the FT-Raman spectrum. The C–N stretching is absorbed at 1244 cm^{-1} and 1250 cm^{-1} in FTIR and FT-Raman spectra, respectively. The CNC deformation vibrational band is observed at 1057 cm^{-1} in the FTIR spectrum. The CNC skeletal deformation vibration is found at 405 cm^{-1} in the FT-Raman spectrum.

3.5.2. DL-malate vibration

The OH stretching vibrations of the carboxylic group observed at about 3300–2500 cm^{-1}, in the formation of hydrogen bonding interaction and super imposed on CH stretching vibrational band [25]. The OH stretching is found as a weak band at 2996 cm^{-1} in the FT-Raman spectrum. The in-plane COH deformation is seen to occur at 1402 cm^{-1} and 1414 cm^{-1} in FTIR and FT-Raman spectra, respectively. The out of plane COH deformation is found at 973 cm^{-1} and 963 cm^{-1} in FTIR and FT-Raman spectrum. The CO$_2$ asymmetric and symmetric stretching vibrations occur in the region 1650-1540 cm^{-1} and 1450-1360 cm^{-1}, respectively. The CO$_2$ asymmetric stretching bands are observed at 1716 cm^{-1} and 1713 cm^{-1} in FTIR and FT-Raman spectra, respectively. The CO$_2$ symmetric stretching vibrational mode is found at 1664 cm^{-1} in the FT-Raman spectrum. The out of plane O–H···O hydrogen bonding deformation is found at 907 cm^{-1} in the FT-Raman spectrum. The OH stretching vibration occurs at about 3550–2500 cm^{-1} when formation of intramolecular hydrogen bonding is involved [27,28]. The hydroxyl group OH stretching is shifted and is found at 3278 cm^{-1} and 3271 cm^{-1} in FTIR and FT-Raman spectra, respectively. This red shift of the stretching wavenumber indicates the formation of weak N–H···O hydrogen bonding, as shown in Fig. 4a. The CO stretching is present at 1156 cm^{-1} in FTIR spectrum. The COH out of plane deformation is found at 648 cm^{-1} and 655 cm^{-1} in FTIR and FT-Raman spectra, respectively. The symmetric CH$_2$ stretching in DL-malate is observed at 2842 cm^{-1} and 2840 cm^{-1} in FTIR and FT-Raman spectra, respectively. The out of plane CH$_2$ wagging deformation is found at 1320 cm^{-1} and 1324 cm^{-1} in FTIR and FT-Raman spectra, respectively. The CH$_2$ in-plane rocking deformation is observed at 783 cm^{-1} in the FT-Raman spectrum. The CH stretching is

Table 2
Optimized geometric parameter of HMTM.

Bond lengths	B3LYP (Å)	XRD (Å)	Bond angles	B3LYP (°)	XRD (°)	Dihedral angles	B3LYP (°)	XRD (°)
H1–O7	1.054	0.996	H3–O2–C13	109.75	109.44	H3–O2–C13–C9	66.13	53.09
H1–O5	1.454	1.394	C12–O4–H15	129.22	123.38	H3–O2–C13–C12	−170.34	176.92
O2–H3	0.978	0.820	H1–O7–C8	112.46	108.35	H3–O2–C13–H14	−53.94	−65.69
O2–C13	1.456	1.420	O6–C8–O7	121.18	120.59	H15–O4–C12–O5	172.85	172.08
O4–C12	1.274	1.230	O6–C8–C9	121.57	121.51	H15–O4–C12–C13	−8.25	−8.01
O4–H15	1.572	1.512	O7–C8–C9	117.23	117.88	C12–O4–H15–N16	−163.61	−174.96
O5–C12	1.293	1.271	C8–C9–H10	106.21	107.81	H1–O7–C8–O6	178.47	178.64
O6–C8	1.244	1.209	C8–C9–H11	108.81	107.82	H1–O7–C8–C9	−0.25	−0.11
O7–C8	1.347	1.307	C8–C9–C13	116.45	117.95	O6–C8–C9–H10	15.90	16.64
C8–C9	1.527	1.516	H10–C9–H11	107.07	107.11	O6–C8–C9–H11	−99.05	−98.70
C9–H10	1.093	0.970	H10–C9–C13	108.51	107.85	O6–C8–C9–C13	136.82	138.98
C9–H11	1.098	0.970	H11–C9–C13	109.38	107.84	O7–C8–C9–H10	−165.38	−164.63
C9–C13	1.552	1.534	O4–C12–O5	123.78	124.26	O7–C8–C9–H11	79.66	80.04
C12–C13	1.539	1.535	O4–C12–C13	120.63	119.66	O7–C8–C9–C13	−44.47	−42.28
C13–H14	1.099	0.980	O5–C12–C13	115.59	116.08	C8–C9–C13–O2	−158.10	−161.20
H15–N16	1.074	0.882	O2–C13–C9	109.67	109.55	C8–C9–C13–C12	81.57	78.92
N16–C17	1.542	1.506	O2–C13–C12	107.77	107.16	C8–C9–C13–H14	−38.22	−42.43
N16–C20	1.545	1.510	O2–C13–H14	109.25	108.77	H10–C9–C13–O2	−38.42	−38.88
N16–C35	1.543	1.508	C9–C13–C12	113.12	113.74	H10–C9–C13–C12	−158.74	−158.76
C17–H18	1.091	0.970	C9–C13–H14	109.54	108.77	H10–C9–C13–H14	81.47	79.90
C17–H19	1.091	0.970	C12–C13–H14	107.41	108.74	H11–C9–C13–O2	78.06	76.49
C17–N29	1.463	1.443	O4–H15–N16	167.88	149.26	H11–C9–C13–C12	−42.27	−43.39
C20–H21	1.091	0.971	H15–N16–C17	110.66	111.99	H11–C9–C13–H14	−162.05	−164.74
C20–H22	1.089	0.970	H15–N16–C20	109.92	108.47	O4–C12–C13–O2	7.19	9.12
C20–N31	1.461	1.441	H15–N16–C35	110.70	110.05	O4–C12–C13–C9	128.60	130.34
C23–H24	1.091	0.970	C17–N16–C20	108.52	108.37	O4–C12–C13–H14	−110.40	−108.30
C23–H25	1.092	0.970	C17–N16–C35	108.52	109.41	O5–C12–C13–O2	−173.82	−170.96
C23–N29	1.496	1.463	C20–N16–C35	108.46	108.45	O5–C12–C13–C9	−52.42	−49.73
C23–N31	1.494	1.452	N16–C17–H18	107.62	109.71	O5–C12–C13–H14	68.58	71.62
C26–H27	1.092	0.970	N16–C17–H19	107.61	109.73	O4–H15–N16–C17	−11.21	−54.13
C26–H28	1.091	0.970	N16–C17–N29	109.24	109.65	O4–H15–N16–C20	108.64	65.43
C26–N29	1.496	1.463	H18–C17–H19	109.91	108.23	O4–H15–N16–C35	−131.56	−176.07
C26–N30	1.494	1.468	H18–C17–N29	111.13	109.74	H15–N16–C17–H18	−59.78	−60.99
N30–C32	1.495	1.463	H19–C17–N29	111.20	109.77	H15–N16–C17–H19	58.62	57.79
N30–C35	1.462	1.448	N16–C20–H21	107.37	109.72	H15–N16–C17–N29	179.46	178.43
N31–C32	1.495	1.462	N16–C20–H22	106.75	109.71	C20–N16–C17–H18	179.54	179.38
C32–H33	1.092	0.970	N16–C20–N31	109.18	109.73	C20–N16–C17–H19	−62.06	−61.83
C32–H34	1.091	0.971	H21–C20–H22	109.99	108.22	C20–N16–C17–N29	58.78	58.80
C35–H36	1.089	0.970	H21–C20–N31	111.12	109.67	C35–N16–C17–H18	61.86	61.31
C35–H37	1.092	0.970	H22–C20–N31	112.21	109.77	C35–N16–C17–H19	−179.74	−179.91
			H24–C23–H25	109.38	107.94	C35–N16–C17–N29	−58.90	−59.27
			H24–C23–N29	109.06	109.2	H15–N16–C20–H21	−59.43	−60.38
			H24–C23–N31	109.20	109.24	H15–N16–C20–H22	58.49	58.39
			H25–C23–N29	109.50	109.22	H15–N16–C20–N31	−179.99	−178.94
			H25–C23–N31	109.50	109.27	C17–N16–C20–H21	61.72	61.43
			N29–C23–N31	110.19	111.89	C17–N16–C20–H22	179.64	179.80
			H27–C26–H28	109.41	107.88	C17–N16–C20–N31	−58.85	−59.25
			H27–C26–N29	109.49	109.27	C35–N16–C20–H21	179.42	179.88
			H27–C26–N30	109.48	109.3	C35–N16–C20–H22	−62.66	−61.12
			H28–C26–N29	109.12	109.26	C35–N16–C20–N31	58.86	59.43
			H28–C26–N30	109.17	109.29	H15–N16–C35–N30	−179.48	−178.06
			N29–C26–N30	110.16	111.75	H15–N16–C35–H36	−58.25	−57.51
			C17–N29–C23	109.90	109.29	H15–N16–C35–H37	59.88	61.42
			C17–N29–C26	109.84	109.08	C17–N16–C35–N30	58.90	58.49
			C23–N29–C26	109.06	108.07	C17–N16–C35–H36	−179.87	−179.03
			C26–N30–C32	109.21	107.91	C17–N16–C35–H37	−61.74	−62.04
			C26–N30–C35	109.94	109.14	C20–N16–C35–N30	−58.82	−59.54
			C32–N30–C35	109.93	109.07	C20–N16–C35–H36	62.42	61.00
			C20–N31–C23	109.93	109.08	C20–N16–C35–H37	−179.45	−179.93
			C20–N31–C32	109.88	109.29	N16–C17–N29–C23	−59.96	−59.11
			C23–N31–C32	109.23	108.07	N16–C17–N29–C26	60.03	58.84
			N30–C32–N31	110.08	111.89	H18–C17–N29–C23	−178.55	−179.40
			N30–C32–H33	109.50	109.24	H18–C17–N29–C26	−58.57	−61.45
			N30–C32–H34	109.14	109.27	H19–C17–N29–C23	58.67	61.77
			N31–C32–H33	109.47	109.22	H19–C17–N29–C26	178.65	179.73
			N31–C32–H34	109.16	109.2	N16–C20–N31–C23	60.09	59.62
			H33–C32–H34	109.46	107.94	N16–C20–N31–C32	−60.15	−59.16
			N16–C35–N30	109.17	109.73	H21–C20–N31–C23	−58.15	−61.03
			N16–C35–H36	106.93	109.72	H21–C20–N31–C32	−178.39	−179.81
			N16–C35–H37	107.53	109.71	H22–C20–N31–C23	178.23	179.81
			N30–C35–H36	111.90	109.77	H22–C20–N31–C32	57.99	61.41
			N30–C35–H37	111.11	109.67	H24–C23–N29–C17	−179.21	−178.71
			H36–C35–H37	110.02	108.22	H24–C23–N29–C26	60.34	62.71

Table 2 (*continued*)

Bond lengths	B3LYP	XRD	Bond angles	B3LYP	XRD	Dihedral angles	B3LYP	XRD
	(Å)	(Å)		(°)	(°)		(°)	(°)
						H25–C23–N29–C17	−59.55	−60.88
						H25–C23–N29–C26	179.99	179.47
						N31–C23–N29–C17	60.94	60.18
						N31–C23–N29–C26	−59.52	−58.40
						H24–C23–N31–C20	179.17	178.46
						H24–C23–N31–C32	−60.20	−62.56
						H25–C23–N31–C20	59.43	60.58
						H25–C23–N31–C32	−179.94	179.56
						N29–C23–N31–C20	−61.06	−60.46
						N29–C23–N31–C32	59.57	58.52
						H27–C26–N29–C17	59.49	61.08
						H27–C26–N29–C23	179.99	179.79
						H28–C26–N29–C17	179.21	178.90
						H28–C26–N29–C23	−60.29	−62.38
						N30–C26–N29–C17	−60.96	−60.00
						N30–C26–N29–C23	59.54	58.72
						H27–C26–N30–C32	179.91	179.89
						H27–C26–N30–C35	−59.40	−61.22
						H28–C26–N30–C32	60.17	62.26
						H28–C26–N30–C35	−179.14	−179.07
						N29–C26–N30–C32	−59.63	−58.83
						N29–C26–N30–C35	61.06	59.83
						C26–N30–C32–N31	59.53	58.52
						C26–N30–C32–H33	179.93	179.57
						C26–N30–C32–H34	−60.26	−62.56
						C35–N30–C32–N31	−61.16	−60.60
						C35–N30–C32–H33	59.24	60.45
						C35–N30–C32–H34	179.04	178.31
						C26–N30–C35–N16	−60.11	−58.26
						C26–N30–C35–H36	−178.27	−178.79
						C26–N30–C35–H37	58.32	62.26
						C32–N30–C35–N16	60.15	59.72
						C32–N30–C35–H36	−58.01	−60.81
						C32–N30–C35–H37	178.57	179.76
						C20–N31–C32–N30	61.16	60.26
						C20–N31–C32–H33	−59.25	−60.78
						C20–N31–C32–H34	−179.06	−178.63
						C23–N31–C32–N30	−59.50	−58.67
						C23–N31–C32–H33	−179.92	−179.71
						C23–N31–C32–H34	60.28	62.44
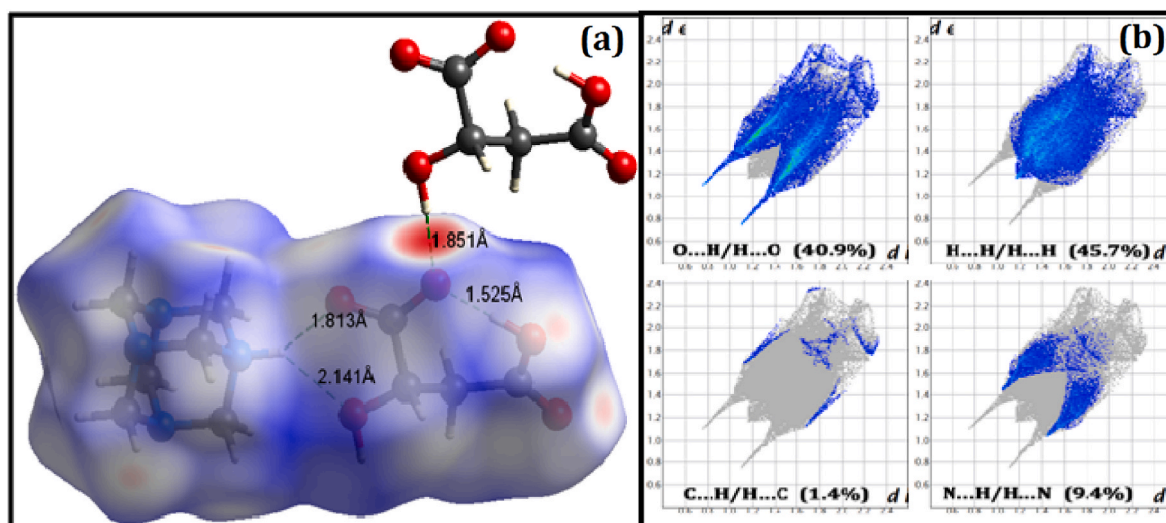
Fig. 4. (a) dnorm mapped Hirshfeld surface plot of HMTM. **(b)** 2D fingerprint plot of HMTM.

observed at 2927 cm^{-1} in the FT-Raman spectrum. The in-plane CCH deformation is found at 1366 cm^{-1} in FTIR spectrum. The in-plane CCH deformation is found at 1366 cm^{-1} in FTIR spectrum. The C–C stretching is found to be 1038 cm^{-1} in FT-Raman and CCC in-plane deformation vibrational modes are observed at 539 cm^{-1} in FTIR and 541 cm^{-1} in

FT-Raman spectrum.

3.6. Natural bond orbital study

Natural bond orbital (NBO) analysis is an effective tool for analyzing
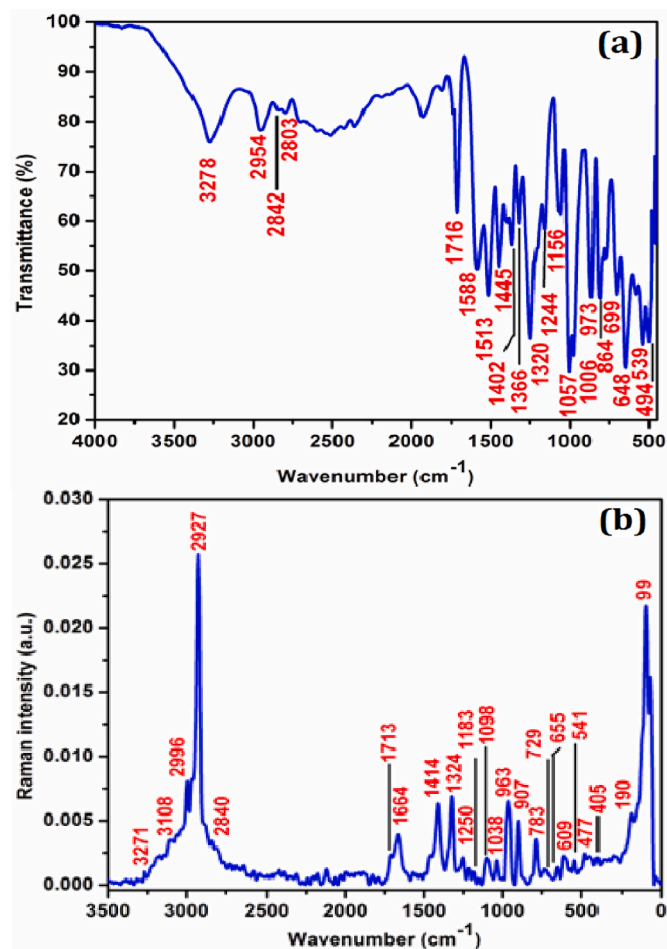
Fig. 5. (a–b). FTIR and FT-Raman spectrum of HMTM.

Table 3

FTIR and FT-Raman vibrational assignments of HMTM.

Wavenumber (cm^{-1})		Vibrational assignment	Wavenumber (cm^{-1})		Vibrational assignment
FTIR	FT-RAMAN		FTIR	FT-RAMAN	
3278	3271	υOH		1098	υCO
	3108	υNH+	1057		δCNC
	2996	υOH		1038	υCC
2954		υasCH2	1006		ρNH+
	2927	υCH	973	963	δCOH
2842	2840	υsymCH2		907	δO-H…O
2803		υsymCH2	864		δO-H…O
1716	1713	υasCO2		783	ρCH2
	1664	υsymCO2		729	ωNH+
1588		γNH+	648	655	δCOH
1513		γNH+		609	δCOH
1445		γCH2	539	541	βCCC
1402	1414	βCOH	494		τCCC
1366		βCCH		477	τCN
1320	1324	ωCH2		405	δCNC
1244	1250	υCN		190	τCCC
	1183	υCN		99	δO-H…O
1156		υCO			

υ: stretching, γ: scissoring, β: inplane bending, ρ: rocking, δ: out of plane bending, ω: wagging, τ: torsion, as: asymmetric, sym: symmetric.

inter and intra-molecular charge transfer interactions and hydrogen bonding interactions. The interactions, with their stabilization energies, specified by second-order perturbation theory analysis, are listed in

Table 4

Second-order perturbation theory analysis of Fock matrix in NBO basis including the stabilization energies of HMTM.

Donor (*i*)	ED(*i*)	Acceptor (*j*)	ED(*j*)	E(2)[a]	E(*j*)-E(*i*)[b]	F(*i*, *j*)[c]
	(e)		(e)	(kJ/mol)	(a.u)	(a.u)
within dl-malate						
σ(H1–O7)	1.98059	σ*(O6–C8)	0.022	24.58	1.27	0.08
σ(C9–H10)	1.97496	σ*(O7–C8)	0.081	18.25	0.91	0.06
σ(C9–H11)	1.96784	π*(O6–C8)	0.248	21.48	0.54	0.05
n2O2	1.96433	σ*(C9–C13)	0.027	22.48	0.69	0.05
n2O2		σ*(C13–H14)	0.028	17.42	0.72	0.05
n1O4	1.95215	σ*(C12–C13)	0.083	27.05	0.97	0.07
n2O4	1.8407	σ*(O5–C12)	0.138	72.77	0.72	0.10
n2O4		π*(O5–C12)	0.295	28.81	0.47	0.05
n2O4		σ*(C12–C13)	0.083	28.09	0.71	0.06
n3O4	1.6266	σ*(O4–C12)	0.053	21.10	0.78	0.06
n3O4		σ*(O5–C12)	0.138	38.60	0.63	0.07
n3O4		π*(O5–C12)	0.295	186.44	0.39	0.12
n1O5	1.96098	σ*(H1–O7)	0.125	39.27	0.99	0.09
n2O5	1.81425	σ*(O4–C12)	0.053	69.33	0.85	0.11
n2O5		σ*(C12–C13)	0.083	26.42	0.69	0.06
n2O6	1.8709	σ*(O7–C8)	0.081	107.94	0.63	0.12
n2O6		σ*(C8–C9)	0.067	69.33	0.61	0.09
n1O7	1.9685	σ*(C8–C9)	0.067	27.09	0.92	0.07
n2O7	1.7657	π*(O6–C8)	0.248	227.18	0.30	0.12
from DL-malate to hexamethylenetetraminium						
n1O2	1.97835	σ*(H15–N16)	0.112	6.39	0.98	0.03
n1O2		σ*(C20–H22)	0.014	5.76	1.02	0.02
n2O2	1.96433	σ*(C35–H36)	0.014	4.13	0.70	0.01
n1O4	1.95215	σ*(H15–N16)	0.112	44.97	0.93	0.09
n2O4	1.8407	σ*(H15–N16)	0.112	176.47	0.67	0.15
within hexamethylenetetraminium						
σ(C17–H18)	1.98487	σ*(C23–N29)	0.040	14.11	0.84	0.05
σ(C17–H19)	1.98483	σ*(C26–N29)	0.039	14.11	0.84	0.05
σ(C20–H21)	1.98459	σ*(N31–C32)	0.039	14.24	0.84	0.05
σ(C20–H22)	1.98429	σ*(C23–N31)	0.039	14.24	0.84	0.05
σ(C35–H36)	1.98452	σ*(C26–N30)	0.039	14.15	0.84	0.05
σ(C35–H37)	1.98479	σ*(N30–C32)	0.039	14.15	0.84	0.05
n1N29	1.87111	σ*(N16–C17)	0.057	45.68	0.52	0.07
n1N29		σ*(C23–N31)	0.039	32.99	0.60	0.06
n1N29		σ*(C26–N30)	0.039	33.08	0.60	0.06
n1N30	1.87042	σ*(N16–C35)	0.058	46.52	0.52	0.07
n1N30		σ*(C26–N29)	0.039	33.37	0.60	0.06
n1N30		σ*(N31–C32)	0.039	33.16	0.60	0.06
n1N31	1.86979	σ*(N16–C20)	0.058	46.93	0.52	0.07
n1N31		σ*(C23–N29)	0.040	33.49	0.60	0.06
n1N31		σ*(N30–C32)	0.039	33.29	0.60	0.06

[a] E(2) - stabilization energy of hyperconjugative interaction.
[b] F(i, j) - Fock matrix element between i and j NBO orbitals.
[c] E(j)-E(i) - Energy difference between donor (i) and acceptor (j) NBO orbitals.

Table 4. The strong intra-molecular charge transfer interaction in the carboxyl group, n2O7→π*(O6–C8) and n3O4→π*(O5–C12) interactions contain high value of electron density, 0.248e and 0.295e, from its π* antibonding orbitals, which leads to stabilization energies of 227.18 and 186.44 kJ/mol, respectively. The dominant N–H⋯O and O–H⋯O intra-molecular hydrogen bonding interactions formed by overlap between nO and σ*(N–H)/σ*(O–H) antibonding orbitals, n2O4→σ*(H15–N16), n1O5→σ*(H1–O7) and n1O4→σ*(H15–N16), have stabilization energies up to 176.47, 39.27 and 44.97 kJ/mol respectively. The σ* (H15–N16) and σ*(H1–O7) antibonding orbitals contain high electron densities of about 0.112e and 0.125e respectively. This high value of electron density causes a slight elongation in the σ*(H15–N16) and σ* (H1–O7) antibonding orbitals. The n→σ* charge transfer interaction, weak N–H⋯O and C–H⋯O hydrogen bonding formed between n1O2→σ*(N16–H15), n1O2→σ*(C20–H22), n2O2→σ*(C35–H36) and n2O2→σ*(C13–H14) antibonding orbitals have stabilization energies up to 6.39, 5.76, 4.13 and 17.42 kJ/mol, respectively. Due to C–H⋯O hydrogen bonding, rehybridization effect leads to the shortening of the C–H bond distance. The n→σ* conjugative interactions between n2O4→σ*(O5–C12) and n2O6→σ*(O7–C8) have stabilization energies of 72.77 and 107.94 kJ/mol, respectively. These intermolecular charge transfer interactions and hydrogen bonding interactions stabilize the HMTM molecule.

3.7. Optical absorption and photoluminescence spectral analysis

The optical properties of the material play an essential role in the photovoltaic conversion mechanism. The UV–visible absorption spectrum of HMTM has strong intense absorption peaks obtained at λ_{max} = 227 nm and 269 nm, which are attributed to n→π* transition. The absorption cut-off wavelength of the HMTM crystal is found to be ~353 nm. It shows a wide transparency window and no considerable absorption in the visible region, which is a noticeable property for NLO applications. The optical band gap energy of the HMTM has been evaluated at 3.52 eV using Tauc's plot [29]. The wide transparency in the visible region and high band gap energy suggests that the HMTM crystal can be a potential material for optoelectronic application. The UV–visible absorption spectrum and Tauc's plot is illustrated in Fig. 6(a-b).

The photoluminescence spectrum of the HMTM crystal has been recorded using the excitation wavelength at 269 nm and the emission spectrum is recorded in the ranges from 290 nm to 500 nm, represented in Fig. 6c. The figure illustrates intense emission peaks at 312 nm and 415 nm, which are observed due to the intermolecular interaction through intermolecular N–H⋯O and O–H⋯O hydrogen bonds with van der Waal's force between Hexamethylenetetraminium and DL-malate within the HMTM crystal. The emission peaks are broadened due to the lattice vibrations in the HMTM crystal. These peaks confirm the blue emission due to lattice vibrations within the HMTM crystal. The calculated excitation band gap energy is 2.99 eV for HMTM crystal. The excitation band gap energy difference from absorption direct band gap energy arises due to Stokes shift of the excitation spectrum in the same electronic transition. The Commission Internationale de L'Eclairage (CIE) coordinates of 0.147 and 0.053, which can be owed to n→π* electron transitions in the various molecular orbital of the HMTM system propose intermolecular charge transfer occurring between hexamethylenetetraminium cation and DL-malate anion. This chromaticity
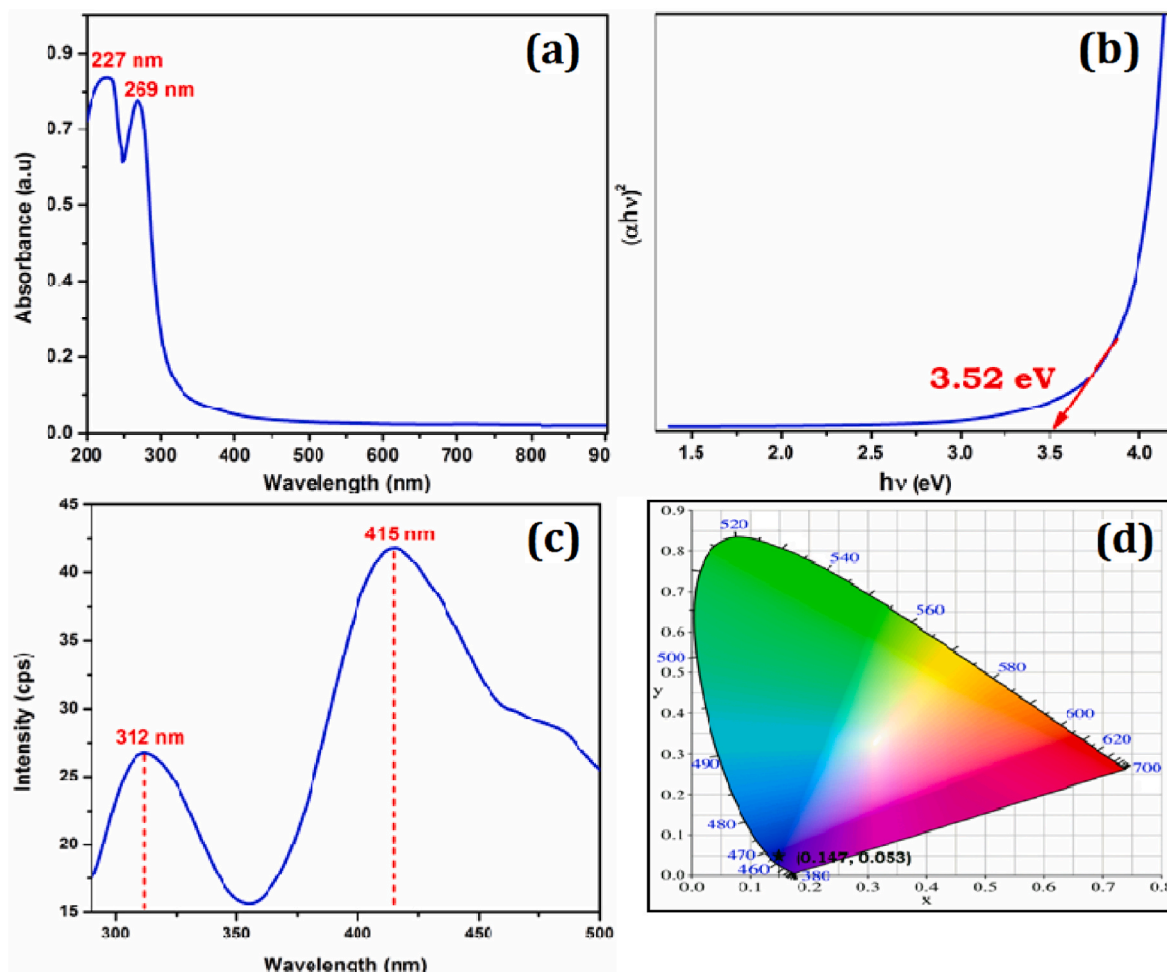
Fig. 6. (a) UV–visible absorption spectrum of HMTM. **(b)** Tauc's plot of HMTM. **(c)** Photoluminescence spectrum of HMTM. **(d)** CIE chromaticity diagram of HMTM.

coordinates of HMTM indicates emission of blue radiation in the visible region. The CIE chromaticity diagram is illustrated in Fig. 6d and it exhibits that this phosphor crystal might be suitable for organic blue light emitting diodes.

3.8. Photoconductivity study

The voltage dependence of photoconductivity in terms of the photocurrent and dark current of the HMTM crystal is carried out by a two probe method at room temperature using a crystal of size $8 \times 4 \times 2$ mm^3. The photoconductivity plot of the HMTM crystal is depicted in Fig. 7a. The dark current is measured by applying voltage in the range of 1–10 V/cm without any electromagnetic radiation and the photocurrent is measured in the same applied voltage range in the presence of electromagnetic radiation falling on the sample. Fig. 7a illustrates that both photocurrent and dark current increase linearly with the applied electric field. From the obtained results, photocurrent (4.99×10^{-5} A) is larger than dark current (2.49×10^{-5} A), which indicates positive photoconductivity of the HMTM crystal. The positive photoconductivity symbolizes the generation of mobile charge carriers in the illumination of electromagnetic radiation, which increase the photocurrent than dark current of the HMTM crystal. This result elucidates lack of traps and intrinsic centre population generated by direct excitation of mobile charge carriers in the title crystal [30].

3.9. Dielectric study

Good quality optically transparent crystal of HMTM of size 8 x 4 x 2 mm^3 has been used for dielectric analysis. The dielectric constant (ε_r) and dielectric loss (ε'') values of the HMTM crystal are high in the low frequency region and low at high frequencies, as illustrated in Fig. 7b and c. The large value of dielectric constant at lower frequencies is related to the contribution of space-charge, orientation, electronic and ionic polarization, and the lower values in the high frequency region is due to the progressive loss of such polarizations, moreover dipoles that cannot pursue the electric fields at all temperatures [31,32]. As temperature increases, dielectric constant decreases; it indicates that the charge carriers are caused by thermal effect [33]. The dielectric constant shows a low value of 8.3 at 393 K. Hence the HMTM can be an appropriate material for electro-optical device applications. The dielectric loss is attributed to the existence of defects and impurities which cause a loss of energy absorbed by the compound. At low frequencies, the slow moving mobile charge carriers cause dielectric loss and it intensely depends on the frequency. At the higher frequencies, the dielectric loss decreases with spatial charge polarization within the HMTM crystal.

From the results, the low value of dielectric constant and dielectric loss at all temperatures indicates that the HMTM crystal has good optical quality and less defects.

3.10. Frontier molecular orbital analysis

The frontier molecular orbital analysis play a vital role in the molecule's optical and electronic properties. The highest occupied molecular orbital (HOMO) and lowest unoccupied molecular orbital (LUMO) of the HMTM are shown in Fig. 8. In the nucleophilic region, HOMO is speared over the hexamethylenetetraminium moiety and in the electrophilic region, LUMO is localized on the entire DL-malate moiety. The energies of HOMO, LUMO and its energy gap are calculated to be −6.434 eV, −1.799 eV and 4.635 eV, respectively. This low value of HOMO-LUMO energy gap indicates the better NLO property of HMTM and it leads to intermolecular charge transfer interaction within the molecule. The calculated values of the global reactivity descriptors, ionisation potential (6.434 eV), electron affinity (1.799 eV), electronegativity (χ) (4.117 eV), chemical hardness (η) (2.317 eV), Global softness (S) (0.216 eV^{-1}), Chemical potential (μ) (−4.117 eV), electrophilicity index (ω) (3.656 eV), total energy change (ΔE_T) (−0.579 eV), and overall energy balance (ΔE) (−4.635 eV) of the HMTM molecule are listed in Table 5.
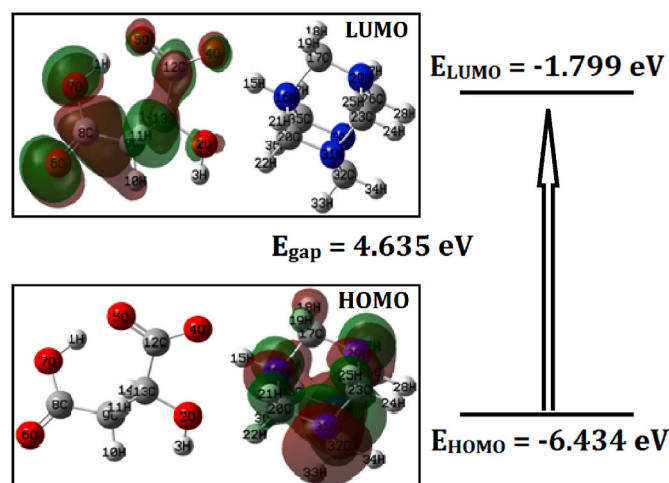
Fig. 8. Frontier molecular orbitals of HMTM.
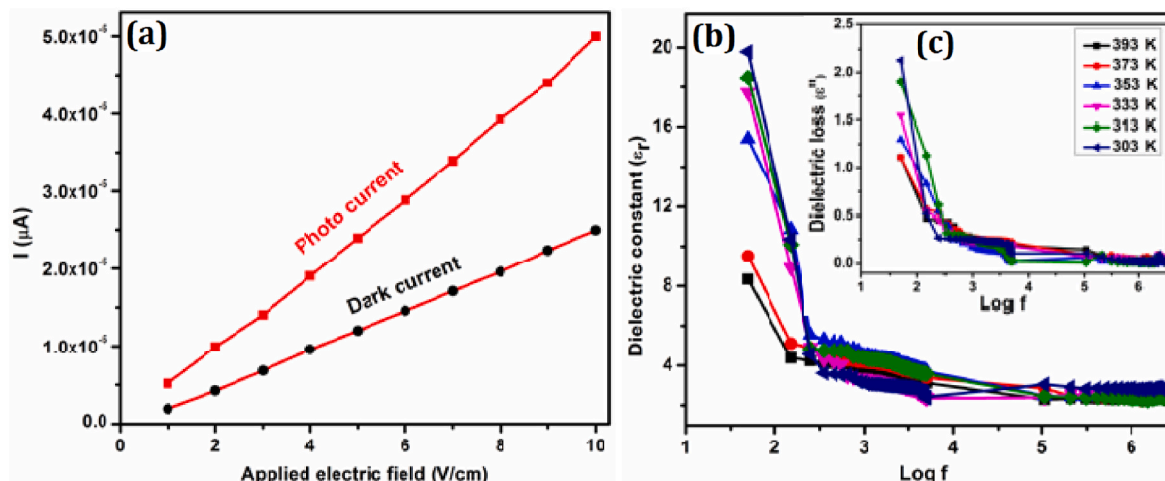
Fig. 7. (a) Photo response of HMTM. **(b)** Dielectric constant of HMTM. **(c)** Dielectric loss of HMTM.

Table 5

Molecular orbital properties of HMTM.

Parameters	B3LYP/6-311++G(d,p)
HOMO energy, E_{HOMO} (eV)	−6.757
LUMO energy, E_{LUMO} (eV)	−2.258
HOMO- LUMO energy gap, ΔE_{GAP} (eV)	4.499
Ionisation potential, IP (eV)	6.757
Electron affinity, EA (eV)	2.258
Electronegativity, χ (eV)	4.508
Chemical hardness, η (eV)	2.249
Global softness, S (eV)$^{-1}$	0.222
Chemical potential, μ (eV)	−4.508
Electrophilicity index, ω (eV)	4.517
Total energy change, ΔE_T (eV)	−0.562
Overall energy balance, ΔE (eV)	−4.499

3.11. MEP surface and natural population analysis

The molecular electrostatic potential (MEP) map is an important tool for investigating molecular reactivity and intermolecular interactions. The MEP is calculated by molecular wavefunction and it is related to the reactivity of the molecule and intermolecular forces [34–38]. The MEP surface was plotted onto isosurface in the range from −0.103 (deepest red) to +0.103 (deepest blue). The electrophilic and nucleophilic reactivity map of HMTM is shown in Fig. 9a. The red region in figure shows the most attractive potential. Electrophilic reactivity is mainly localized on electronegative oxygen atom in DL-malate anion and nitrogen atoms in hexamethylenetetraminium cation due to the lone pairs as well as π-electrons. Whereas the blue region indicates the most repulsive potential, nucleophilic reactivity is mainly localized on hydrogen and carbon atoms of HMTM molecule due to the partial shielding of the nuclear charge density.

Natural population analysis is a tool used to determine the electronic configuration and the net atomic charge associated with each atom in a polyatomic molecule. The H3 atom attached with O2 atom in the hydroxyl group contains maximum negative charge of −0.781e, due to N–H⋯O and O–H⋯O hydrogen bonded oxygen atoms, O4 and O5 atoms hold the high negative charges −0.758e and −0.718e, respectively. The oxygen atom attached and hydrogen bonded hydrogen atoms, H1, H15 and H3 atoms have positive charges of 0.495e, 0.495e and 0.462e, respectively. The oxygen attached carboxylic group carbon atoms, C17 and C8 have maximum positive charges of 0.797e and 0.791e respectively. The hydrogen and carbon attached C9 atom has a negative charge of −0.506e. All carbon atoms except C9 atom contain positive charges (0.006e–0.035e) due to the attachment of nitrogen atom in hexamethylenetetramine moiety. The oxygen atoms, O6 and O7, have the negative charges of −0.625e and −0.711e, respectively. All hydrogen atoms have positive charges in the range from 0.191e to 0.231e. The nitrogen atoms, N16, N29, N30 and N31 in the hexamethylenetetraminium moiety contain negative charges between −0.565e and −0.571e. The

theoretically calculated net atomic charges of the HMTM polyatomic molecule are illustrated in Fig. 9b.

3.12. NLO studies

3.12.1. Second harmonic generation study

The second harmonic generation (SHG) efficiency of the powdered HMTM crystal has been determined using the modified Kurtz and Perry technique [39]. A Q-switched Nd:YAG laser beam (1064 nm) with a pulse width of 6 ns is used as an optical source. The powdered HMTM crystal emits green radiation of wavelength 532 nm which confirms the SHG behavior. Photomultiplier tube converts the green light intensity into electrical signals. The SHG efficiency produced is found to be 3.6 mJ for powdered HMTM crystals and 1.6 mJ for powdered potassium dihydrogen phosphate (KDP), respectively. Thus, the relative NLO efficiency of the powdered HMTM crystal is 1.25 times greater than that of powdered KDP.

3.12.2. Z-scan and optical limiting studies

Fig. 10a shows a sketch of the open aperture z-scan arrangement and Fig. 10b shows the plot of closed aperture z-scan arrangement of the HMTM complex. Fig. 10c represents the ratio of values obtained from closed aperture and open aperture arrangements. Also, the data obtained from this technique noticeably demonstrates the nonlinear refraction.

The measurable quantity ΔT_{p-v}, is the difference between the peak transmittance and valley transmittance values, T_p-T_v and is a function of $|\Delta\phi|$ is given by

$$\Delta T_{p-v} = 0.406\,(1-s)^{0.25}\,|\Delta\phi| \tag{1}$$

where $\Delta\phi$ is the on-axis phase shift and S is the linear aperture transmittance given by

$$S = 1 - exp(\frac{-2r_a^2}{\omega_a^2}) \tag{2}$$

where r_a is the radius of the aperture and ω_a is the beam radius at the aperture. The on axis phase shift ($\Delta\phi$) is related to the third order nonlinear refractive index (n_2),

$$n_2 = \frac{\Delta\phi}{kI_0L_{eff}} \tag{3}$$

where k = 2π/λ, λ is the wavelength of laser beam used.

α is the linear absorption coefficient,
L is the thickness of the specimen,
I_0 is the on-axis irradiance at focus (31.3 × 10^2 W/cm^2)
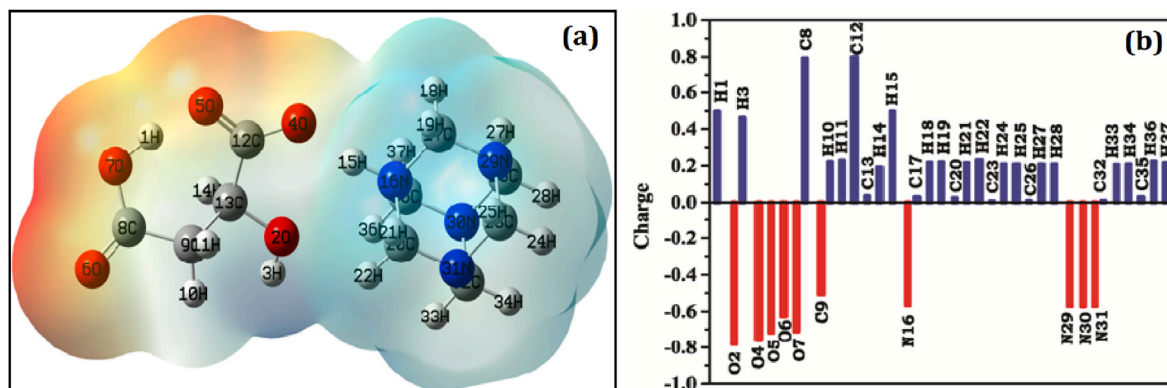
Fig. 9. (a) MEP surface map of HMTM. **(b)** Natural population atomic charge of HMTM.
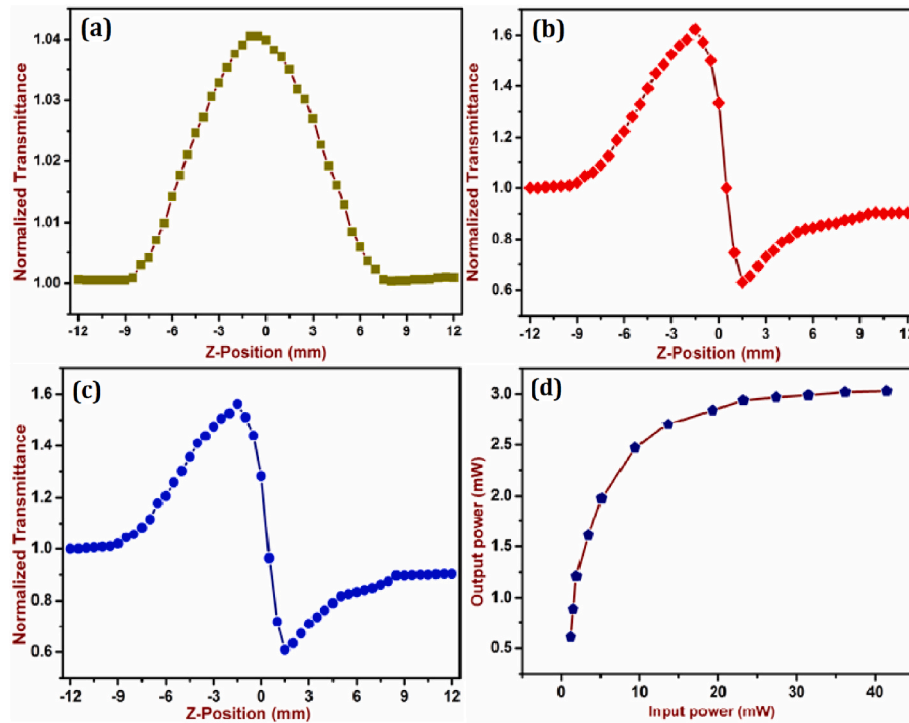
Fig. 10. (a) Open aperture of HMTM. (b) Closed aperture of HMTM. (c) Ratio of open and closed aperture. (d) Optical limiting curve of HMTM.

L $_{eff}$ = [1 – exp (−α L)]/α, is the effective thickness of the specimen,

$$L_{eff} = \frac{1 - e^{(-\alpha L)}}{\alpha} \tag{4}$$

The enhanced values of transmittance observed at the focus gives evidence for saturated behavior of absorption at elevated intensity limits, as shown in open aperture arrangement plot (Fig. 10a). From closed aperture arrangement, owing to the sample saturation behavior, the peak increases and valley decreases, as a result of symmetry nature, Z-scan plot is changed at Z = 0, [40].

From Open aperture Z-scan arrangement, the nonlinear absorption coefficient can be estimated as,

$$\beta = \frac{2\sqrt{2}\,\Delta T}{I_0 L_{eff}} \text{cmW}^{-1} \tag{5}$$

Herein ΔT is one valley value at the open aperture Z-scan plot.

The real and imaginary parts of the third order nonlinear optical susceptibility could be determined from the experimental calculation of n_2 and β according to the following relations [41,42],

$$Re\chi^{(3)}(esu) = 10^{-4} \frac{\left(\varepsilon_o C^2 n_o^2 n^2\right)}{\pi} \left(\frac{cm}{W}\right) \tag{6}$$

$$Im\chi^{(3)}(esu) = 10^{-2} \frac{\left(\varepsilon_o C^2 n_o^2 \lambda \beta\right)}{4\pi^2} \left(\frac{cm}{W}\right) \tag{7}$$

The absolute value of $\chi^{(3)}$ was calculated from the following relation.

$$|\chi^{(3)}| = \left[\left(Re\chi^{(3)}\right)^2 + \left(Im\chi^{(3)}\right)^2 \right]^{\frac{1}{2}} \tag{8}$$

The estimated Z-scan results are shown in Table 6. From the results attained, it is understood that the negative value of nonlinear refraction exposed by the sample is due to self-defocusing behavior of the complex. It is also noted that the localized heating evolved in the sample owing to continuous exposure of the sample to the laser eventually results in the change in refractive index. Additionally, the intensity dependent refractive index in the complex could result in self defocusing (Kerr effect) giving rise to negative nonlinearity [42,43]. From Fig. 10b, it could

Table 6
Evaluated third order nonlinear properties of HMTM.

Laser beam wavelength (λ)	532 nm
Laser power (P)	34.3 mw
Lens Focal length (f)	3.5 cm
Optical path difference (Z)	700 mm
Radius of the aperture	2 mm
Beam radius at the aperture	15 mm
Incident intensity at the focus (Z = 0)	4.35 kW/cm^2
Nonlinear refractive index (n_2)	-4.112×10^{-8} cm^2/W
Nonlinear absorption coefficient (β)	0.041×10^{-4} cm^2/W
Real part of Third-order nonlinear susceptibility (Re $\chi^{(3)}$)	2.167×10^{-6} esu
Imaginary part of Third-order nonlinear susceptibility (Im $\chi^{(3)}$)	0.171×10^{-6} esu
Third-order nonlinear susceptibility ($\chi^{(3)}$)	2.179×10^{-6} esu

also be observed that the β value exposed material's saturation absorption behavior enable the material to be extremely beneficial in optical limiting applications. Consequently, the optical limiting threshold of the title crystal and the corresponding received output clamping data values are estimated with the data values presented in Fig. 10d and are found to be about 23.2 mW and 2.94 mW respectively [42].

3.12.3. First- and second-order hyperpolarizability studies

The NLO properties of HMTM are enhanced due to the existence of N–H⋯O and O–H⋯O hydrogen bonds [44,45]. The high value of first-, second-order hyperpolarizability, isotropic-, anisotropic polarizability and dipole moment of the title molecule indicate considerable NLO properties. The dipole moment (μ_{total}) of the HMTM molecule is computed to be 17.41 Debye. The larger values of molecular dipole moment relative to reference KDP crystal show the large NLO property of HMTM molecule. The static polarizabilities $\alpha(0;0)$ and the frequency dependent dynamic polarizabilities $\alpha(-\omega;\omega)$ of the HMTM molecule have been calculated. The static and dynamic, isotropic (α) poloarizablities are calculated to be 20.77×10^{-24} esu and 20.90×10^{-24} esu, respectively, and the respective anisotropic $(\Delta\alpha)$ polarizability values are simulated to be 9.10×10^{-24} esu and 9.22×10^{-24} esu. The static first

hyperpolarizability β(0; 0,0), frequency dependent first hyperpolarizability using quadratic electro-optic Kerr effect β(-ω; ω,0) and dynamic first hyperpolarizability using electric field induced second harmonic generation (EFISH) β(-2ω; ω,ω) are calculated to be 2.29×10^{-30} esu, 2.39×10^{-30} esu and 2.58×10^{-30} esu respectively, this is 8.41, 8.54 and 8.89 times greater than that of urea (β(0; 0,0) = 0.27×10^{-30} esu, β(-ω; ω,0) = 0.28×10^{-30} esu, β(-2ω; ω,ω) = 0.29×10^{-30} esu). The dipole orientation static second hyperpolarizabilities γ(0; 0,0, 0) are calculated to be 6.29×10^{-36} esu for HMTM and 0.73×10^{-36} esu for urea. The frequency dependent second hyperpolarizabilities γ(-ω; ω,0,0) using the quadratic electro-optic Kerr effect are 6.66×10^{-36} esu and 0.77×10^{-36} esu for HMTM and urea, respectively. Using EFISH, the calculated dynamic second hyperpolarizability value of HMTM is 7.46×10^{-36} esu and that of urea is 0.84×10^{-36} esu. These second hyperpolarizability γ(0; 0,0,0), γ(-ω; ω,0,0) and γ(-2ω; ω,ω,0) values are respectively 8.62, 8.65 and 8.88 times greater than those of urea.

4. Conclusion

Nonlinear optical single crystal of Hexamethylenetetraminium hydrogen DL-malate was successfully grown by solvent slow evaporation method at room temperature using methanol as solvent. The HMTM crystal belongs to monoclinic crystal system with non-centrosymmetric Cc space group as identified from single crystal X-ray diffraction analysis. The PXRD pattern confirms the phase and crystalline nature. The structural and vibrational properties are confirmed and investigated by ^{1}H, ^{13}C NMR, FTIR and FT-Raman analyses. The intermolecular charge transfer N–H⋯O and O–H⋯O hydrogen bonding interactions and element-element intercontacts are confirmed by Hirshfeld surface study. The existence of N–H⋯O and O–H⋯O hydrogen bonds due to n→π* intra-molecular charge transfer interactions between lone pair of oxygen with N–H and O–H antibonding orbitals are confirmed by NBO analysis. From the UV–visible spectrum, the lower cut-off wavelength is obtained at 353 nm and no considerable absorption is noted in the visible region, which is a pronounced property for NLO applications. The optical band gap energy of the title crystal is predicted to be 3.52 eV using Tauc's plot. HMTM exhibits blue emission confirmed by photoluminescence study. The low dielectric constant, dielectric loss and positive photoconductivity of the HMTM crystal indicate that it is a suitable candidate for optoelectronic applications. The electronic structural properties of HMTM have been investigated using NBO, HOMO-LUMO, NPA and MEP surface analysis. The relative SHG efficiency of the powdered HMTM crystal is obtained to be 1.25 times greater than that of KDP. The Z-scan analysis confirmed the self-defocusing nature of HMTM. From optical limiting study, the optical limiting threshold and output clamping are found to be 23.2 mW and 2.94 mW, respectively. Optical limiting study reveals the title crystal to be useful in low power optical limiting applications. The high values of first- and second-order hyperpolarizabilities of the HMTM molecule indicate considerable NLO property and its suitability in nonlinear optical applications. Therefore, the aforesaid investigations establish that HMTM crystal could be a promising candidate for both second and third-order NLO applications.

CRediT authorship contribution statement

M. Saravanakumar: Formal analysis, Methodology, Writing – original draft. **J. Chandrasekaran:** Conceptualization, Supervision, Validation. **M. Krishnakumar:** Formal analysis. **G. Vinitha:** Writing – review & editing. **Mohd Anis:** Writing – review & editing.

Declaration of competing interest

The authors declare that they have no known competing financial interests or personal relationships that could have appeared to influence the work reported in this paper.

References

[1] H.S. Nalwa, S. Miyata, Nonlinear Optics of Organic Molecules and Polymers, CRC Press, New york, 1996.

[2] P. Narayana Prasad, D.J. Williams, Introduction to Nonlinear Optical Effects in Molecules and Polymers, Wiley, New york, 1990.

[3] T.C. Sabari Girisun, S. Dhanuskodi, Nonlinear optical susceptibilities of diglycinyl thiourea for frequency conversion and optical limiting applications, Chem. Phys. Lett. 491 (2010) 248–253, https://doi.org/10.1016/j.cplett.2010.04.014.

[4] Z. Li, K. Wu, G. Su, Y. He, Nonlinear optical properties of some derivatives of stilbene and vinyl cyanide, Opt. Mater. 20 (2002) 295–299, https://doi.org/10.1016/S0925-3467(02)00072-1.

[5] M.K. Marchewka, S. Debrus, H. Ratajczak, Vibrational spectra and second harmonic generation in molecular complexes of L-lysine with L-tartaric, D,L-Malic, acetic, arsenous, and fumaric acids M, Cryst. Growth Des. 3 (2003) 587–592, https://doi.org/10.1021/cg030008v.

[6] Z. Kotler, R. Masse, R. Hierle, D. Josse, J. Zyss, Quadratic nonlinear-optical properties of a new transparent and highly efficient organic–inorganic crystal: 2-amino-5-nitropyridinium-dihydrogen phosphate (2A5NPDP), J. Opt. Soc. Am. B 9 (1992) 534, https://doi.org/10.1364/JOSAB.9.000534.

[7] N. Sudharsana, B. Keerthana, R. Nagalakshmi, V. Krishnakumar, L. Guru Prasad, Growth and characterization of hydroxyethylammonium picrate single crystals for third-order nonlinear optical applications, Mater. Chem. Phys. 134 (2012) 736–746, https://doi.org/10.1016/j.matchemphys.2012.03.062.

[8] G.R. Desiraju, G.W. Parshall, Crystal engineering: the design of organic solids, Mater. Sci. Monogr. 54 (1989).

[9] M. Saravanakumar, J. Chandrasekaran, M. Krishnakumar, B. Babu, G. Vinitha, M. Anis, Experimental and quantum chemical studies on SHG, Z-scan and optical limiting investigation of 2-amino-5-bromopyridinium trifluoroacetate single crystal for optoelectronic applications, J. Phys. Chem. Solid. 136 (2020), 109133, https://doi.org/10.1016/j.jpcs.2019.109133.

[10] K. Biradha, G. Mahata, Enclathration of aromatic molecules by the O-H⋯N supramolecular adducts of racemic-bis-β-naphthol and 4,4′-bipyridine, Cryst. Growth Des. 5 (2005) 61–63, https://doi.org/10.1021/cg049761u.

[11] S. Vijayalakshmi, S. Kalyanaraman, Non linear optical analyses of hexamine: phenol cocrystals based on hydrogen bonding: a comparative study, Spectrochim. Acta Part A Mol. Biomol. Spectrosc. 120 (2014) 14–18, https://doi.org/10.1016/j.saa.2013.10.006.

[12] R. Padmavathy, N. Karthikeyan, D. Sathya, R. Jagan, R. Mohan Kumar, K. Sivakumar, Anion assisted supramolecular self-assemblies of succinate and malate adducts: crystal structures and theoretical modelling, RSC Adv. 6 (2016) 68468–68484, https://doi.org/10.1039/C6RA15683E.

[13] J.E. Bertie, M. Solinas, Infrared and Raman spectra and the vibrational assignment of hexamethylenetetramine- h 12 and - d 12, J. Chem. Phys. 61 (1974) 1666–1677, https://doi.org/10.1063/1.1682160.

[14] P.S. Santos, Raman spectra of some adducts of hexamethylenetetramine, J. Raman Spectrosc. 20 (1989) 405–408, https://doi.org/10.1002/jrs.1250200702.

[15] S. Chandrasekhar, S. Mukherjee, Salts of hexamethylenetetramine with organic acids: enhanced anomeric interactions with a lowering of molecular symmetry revealed by crystal structures, J. Mol. Struct. 1082 (2015) 188–194, https://doi.org/10.1016/j.molstruc.2014.11.013.

[16] G. Rauhut, P. Pulay, Transferable scaling factors for density functional derived vibrational force fields, J. Phys. Chem. 99 (1995) 3093–3100, https://doi.org/10.1021/j100010a019.

[17] M.J. Frisch, G.W. Trucks, H.B. Schlegel, G.E. Scuseria, M.A. Robb, J.R. Cheeseman, G. Scalmani, V. Barone, G.A. Petersson, H. Nakatsuji, M.C.X. Li, A. Marenich, J. Bloino, B.G. Janesko, R. Gomperts, B. Mennucci, H.P. Hratchian, J.V. Ort, D. J. Fox, Gaussian 09, Revision C.01, Gaussian Inc., Wallingford CT, 2010.

[18] A.D. Becke, Density-functional thermochemistry. III. The role of exact exchange, J. Chem. Phys. 98 (1993) 5648–5652, https://doi.org/10.1063/1.464913.

[19] E.D. Glendening, A.E. Reed, J.E. Carpenter, F. Weinhold, NBO, Version 3.1, TCI, University of Wisconsin, Madison, 1998.

[20] J. Chocholoušová, V. Špirko, P. Hobza, First local minimum of the formic acid dimer exhibits simultaneously red-shifted O-H⋯O and improper blue-shifted C-H⋯O hydrogen bonds, Phys. Chem. Chem. Phys. 6 (2004) 37–41, https://doi.org/10.1039/b314148a.

[21] M. Szafran, A. Komasa, E. Bartoszak-Adamska, Crystal and molecular structure of 4-carboxypiperidinium chloride (4-piperidinecarboxylic acid hydrochloride), J. Mol. Struct. 827 (2007) 101–107, https://doi.org/10.1016/j.molstruc.2006.05.012.

[22] R. Dennington, T.A. Keith, J.M. Millam, K. Eppinnett, W. Hovell, Gauss View, Version 5.0, Semichem Inc., Shawnee Mission, 2003.

[23] S.K. Wolff, D.J. Grimwood, J.J. McKinnon, M.J. Turner, D. Jayatilaka, M. A. Spackman, Crystal Explorer, Version 3.1, University of Western Australia, Western Australia, 2012.

[24] G. Socrates, Infrared and Raman Characteristic Group Frequencies. Tables and Charts, third ed., John Wiley and Sons Ltd, England, 2001.

[25] N.B. Colthup, L.H. Daly, S.E. Wiberley, Introduction to Infrared and Raman Spectroscopy, third ed., Academic Press Inc, New York, 1990.

[26] W.B. Wright, The C-H stretching bands of aliphatic amines, J. Org. Chem. 24 (1959) 1362–1363, https://doi.org/10.1021/jo01091a619.

[27] G. Dhanaraj, M.R. Srinivasan, H.L. Bhat, Vibrational spectroscopic study of L-arginine phosphate monohydrate (LAP), a new organic non-linear crystal, J. Raman Spectrosc. 22 (1991) 177–181, https://doi.org/10.1002/jrs.1250220307.

[28] D. Lin-Vien, N.B. Colthup, W.G. Fateley, J.G. Grasselli, The Handbook of Infrared and Raman Characteristic Frequencies of Organic Molecules, first ed., Academic Press, New york, 1991.

[29] J. Tauc (Ed.), Amorphous and Liquid Semiconductors, Plenum Press, New york, 1974.

[30] R.H. Bube, Photoconductivity of Solids, second ed., Wiley Interscience, New york, 1960.

[31] F. Kremer, A. Schönhals, Broadband Dielectric Spectroscopy, Springer-Verlag Berlin Heidelberg, New york, 2002.

[32] K. Syed Suresh Babu, G. Peramaiyan, M. Nizammohideen, R. Mohan, Crystal structure, growth and characterizations of semiorganic nonlinear optical (Bis) isonicotinamide perchlorate monohydrate (BINPM), J. Therm. Anal. Calorim. 120 (2015) 1337–1345, https://doi.org/10.1007/s10973-015-4457-8.

[33] S. Nazarath Begum, U. Sankar, T. Chithambrathanu, P. Selvarajan, Growth, structural, mechanical, thermal and dielectric characterization of Triglycine sulpho-picrate (Tgspi) single crystals, Optik (Stuttg). 125 (2014) 1493–1497, https://doi.org/10.1016/j.ijleo.2013.09.023.

[34] E. Scrocco, J. Tomasi, Electronic Molecular Structure, Reactivity and Intermolecular Forces: an Euristic Interpretation by Means of Electrostatic Molecular Potentials, 1978, https://doi.org/10.1016/S0065-3276(08)60236-1.

[35] Jorge M. Seminario, Recent Developments and Applications of Modern Density Functional Theory, first ed., Elsevier Science, New york, 1996.

[36] P. Politzer, D.G. Truhlar (Eds.), Chemical Applications of Atomic and Molecular Electrostatic Potentials, first ed., Plenum Press, New york, 1981.

[37] J.S. Murray, P. Politzer, Electrostatic potentials of amine nitrogens as a measure of the total electron-attracting tendencies of substituents, Chem. Phys. Lett. 152 (1988) 364–370, https://doi.org/10.1016/0009-2614(88)80107-6.

[38] P. Politzer, K. Jayasuriya, P. Sjoberg, P.R. Laurence, Properties of some possible intermediate stages in the nitration of benzene and toluene, J. Am. Chem. Soc. 107 (1985) 1174–1177, https://doi.org/10.1021/ja00291a015.

[39] S.K. Kurtz, T.T. Perry, A powder technique for the evaluation of nonlinear optical materials, J. Appl. Phys. 39 (1968) 3798–3813, https://doi.org/10.1063/1.1656857.

[40] B. Dhanalakshmi, S. Ponnusamy, C. Muthamizhchelvan, V. Subhashini, Growth and characterization of a third order nonlinear optical single crystal: ethylenediamine-4-nitrophenolate monohydrate, Mater. Res. Bull. 70 (2015) 809–816, https://doi.org/10.1016/j.materresbull.2015.06.020.

[41] I.P. Bincy, R. Gopalakrishnan, Synthesis, growth and characterization of new organic crystal: 2-Aminopyridinium p-Toluenesulfonate for third order nonlinear optical applications, J. Cryst. Growth 402 (2014) 22–31, https://doi.org/10.1016/j.jcrysgro.2014.03.024.

[42] M. Krishnakumar, S. Karthick, G. Vinitha, K. Thirupugalmani, B. Babu, S. Brahadeeswaran, Growth, structural, linear, nonlinear optical and laser induced damage threshold studies of an organic compound: 2-Amino pyridinium-4-hydroxy benzoate, Mater. Lett. 235 (2019) 35–38, https://doi.org/10.1016/j.matlet.2018.09.148.

[43] R. Westlund, E. Glimsdal, M. Lindgren, R. Vestberg, C. Hawker, C. Lopes, E. Malmström, Click chemistry for photonic applications: triazole-functionalized platinum(ii) acetylides for optical power limiting, J. Mater. Chem. 18 (2008) 166–175, https://doi.org/10.1039/b711269f.

[44] D. Xue, S. Zhang, Chemical bond analysis of nonlinearity of urea crystal, J. Phys. Chem. A. 101 (1997) 5547–5550, https://doi.org/10.1021/jp962541+.

[45] P.K. Nandi, K. Mandal, T. Kar, Effect of structural changes in sesquifulvalene on the intramolecular charge transfer and nonlinear polarizations - a theoretical study, Chem. Phys. Lett. 381 (2003) 230–238, https://doi.org/10.1016/j.cplett.2003.09.135.